scientific reports

Check for updates

OPEN

Glioblastoma mesenchymal subtype enhances antioxidant defence to reduce susceptibility to ferroptosis

Simona D'Aprile[1], Simona Denaro[1], Alessandro Lavoro[1], Saverio Candido[1], Sebastiano Giallongo[1], Filippo Torrisi[2], Lucia Salvatorelli[3], Giacomo Lazzarino[4], Angela Maria Amorini[1], Giuseppe Lazzarino[1], Gaetano Magro[3], Daniele Tibullo[1], Massimo Libra[1], Cesarina Giallongo[3]✉, Nunzio Vicario[1]✉ & Rosalba Parenti[1]

Glioblastoma (GBM) represents an aggressive brain tumor, characterized by intra- and inter-tumoral heterogeneity and therapy resistance, leading to unfavourable prognosis. An increasing number of studies pays attention on the regulation of ferroptosis, an iron-dependent cell death, as a strategy to reverse drug resistance in cancer. However, the debate on whether this strategy may have important implications for the treatment of GBM is still ongoing. In the present study, we used ferric ammonium citrate and erastin to evaluate ferroptosis induction effects on two human GBM cell lines, U-251 MG, with proneural characteristics, and T98-G, with a mesenchymal profile. The response to ferroptosis induction was markedly different between cell lines, indeed T98-G cells showed an enhanced antioxidant defence, with increased glutathione levels, as compared to U-251 MG cells. Moreover, using bioinformatic approaches and analysing publicly available datasets from patients' biopsies, we found that GBM with a mesenchymal phenotype showed an up-regulation of several genes involved in antioxidant mechanisms as compared to proneural subtype. Thus, our results suggest that GBM subtypes differently respond to ferroptosis induction, emphasizing the significance of further molecular studies on GBM to better discriminate between various tumor subtypes and progressively move towards personalized therapy.

Keywords Glioblastoma, Ferroptosis, Iron overload, Erastin, Proneural subtype, Mesenchymal subtype

Abbreviations

AUC	Area under curve
BH4	Tetrahydrobiopterin
Cl Casp3	Cleaved Caspase-3
CoQ10	Coenzyme Q10
DMSO	Dimethyl sulfoxide
DHFR	Dihydrofolate reductase
FAC	Ferric ammonium citrate
FITC	Fluorescein isothiocyanate
FSP1	Ferroptosis suppressor protein 1
GBM	Glioblastoma
GCH1	GTP cyclohydrolase I
GEO	Gene Expression Omnibus
GPX4	Glutathione peroxidase 4
GSH	Glutathione
H2-DCF	2',7'-Dichlorodihydrofluorescein acetate

[1]Department of Biomedical and Biotechnological Sciences, University of Catania, 95123 Catania, Italy. [2]Department of Medicine and Surgery, University of Enna "Kore", 94100 Enna, Italy. [3]Department of Medical and Surgical Sciences and Advanced Technologies, F. Ingrassia, University of Catania, 95123 Catania, Italy. [4]Departmental Faculty of Medicine, UniCamillus-Saint Camillus International University of Health Sciences, Via Di Sant'Alessandro 8, 00131 Rome, Italy. ✉email: cesarina.giallongo@unict.it; nunziovicario@unict.it

LDH	Lactate dehydrogenase
MTT	3-(4,5-Dimethylthiazol-2-yl)-2,5-diphenyltetrazolium bromide
OS	Overall survival
PBS	Phosphate-buffered saline
PFI	Progression free interval
PUFAs	Polyunsaturated fatty acids
ROS	Reactive oxygen species
TfR1	Type I transferrin receptor
WHO	World Health Organization

Glioblastoma (GBM), a grade IV malignant primary brain tumor, is the most aggressive central nervous system (CNS) cancer, with a poor prognosis for patients[1–3]. To date standard therapeutic approach relies on surgery, radiotherapy, and chemotherapy; however, typical GBM heterogeneity significantly hampers therapeutic effectiveness[4,5]. Beyond inter-patient variability, intra-tumoral heterogeneity is also a critical feature of this dismal disease[6]. Therefore, a large-scale genomic analysis grouped GBM into 3 principal subtypes: classical, proneural and mesenchymal, harbouring different characteristics and features[7,8]. Mesenchymal tumors usually display the worst prognosis, eventually providing an increased therapy resistance as compared to proneural subtype[9–11]. For this reason, additional studies are needed to investigate the impact of GBM heterogeneity on the identification of new therapeutic targets and to develop personalized approaches[12–14].

Ferroptosis is an iron-dependent cell death related to increased intracellular reactive oxygen species (ROS) and subsequent phospholipid peroxidation[15]. The mechanisms triggering ferroptosis cascade are strictly related to iron uptake and handling, along with redox homeostasis and mitochondrial activity[16–18]. The antioxidant system xc−/glutathione (GSH)/glutathione peroxidase 4 (GPX4) axis is considered one of the key elements in regulating ferroptosis[19].

Interestingly, recent studies reported that ferroptosis could be a promising therapeutic strategy to counteract tumor proliferation and invasiveness[20–22]. Moreover, within the CNS, the activity of antioxidant enzymes is relatively lower as compared to other tissues, while polyunsaturated fatty acids (PUFAs) amount is higher, increasing vulnerability to oxidative stress and lipid peroxidation[23,24]. Such a susceptibility that characterizes neural-derived cells, support ferroptosis and redox-balance as a potential therapeutic strategy for GBM. Indeed, some studies reported that ferroptosis induction in GBM reduced cancer cells growth, partially improving radiotherapy and chemotherapy efficacy[25]. However, the response to ferroptosis inducers can differ, meaning that some tumoral types or subtypes may exhibit resistance to this programmed cell death[26]. Ferroptosis activation may be limited by GBM heterogeneity, hypoxia and a complex and diversified immune microenvironment[27–29]. Moreover, metabolic reprogramming of GBM microenvironment could affect resistance mechanisms to ferroptosis. Therefore, understanding these mechanisms, it could be of critical importance in overcoming the limiting factors of potential therapeutic strategies[30].

Herein, we analysed GBM susceptibility to ferroptosis by exposing U-251 MG and T98-G human GBM cell lines, as proneural or mesenchymal GBM cell lines respectively, to ferric ammonium citrate (FAC)-mediated iron overload and erastin, a ferroptosis activator. We also analysed available datasets of GBM human biopsies, finding that mesenchymal GBM phenotypes showed up-regulated genes coding for antioxidant enzymes as compared to proneural subtype, confirming a better antioxidant profile in mesenchymal tumors and greater resistance towards ferroptosis.

Results

T98-G cells tolerate ferroptosis induction

Firstly, we assessed proliferative potential of U-251 MG and T98-G cells. We found that the two cell lines showed superimposable doubling time, thus ruling out potential differences in cell growth rate (Figure S1). Through MTT assay, we tested increasing FAC concentrations (5, 10, 20, 50, 100 µM) at 24 or 48 h post-treatment to evaluate its effects on U-251 MG and T98-G metabolic turnover (Fig. 1). At 24 h, our analysis did not detected significant changes of MTT turnover in U-251 MG cells at any tested FAC concentrations as compared to untreated controls; instead, at 48 h post-treatment, we observed a significant reduction of MTT turnover of about 20% starting from 5 µM up to 100 µM of FAC treatment (70.95 ± 6.20, p-value = 0.0092 for 5 µM FAC-treated U-251 MG; 76.06 ± 2.58, p-value = 0.0378 for 10 µM FAC-treated U-251 MG; 65.22 ± 4.19, p-value = 0.0018 for 20 µM FAC-treated U-251 MG; 73.77 ± 5.15, p-value = 0.0205 for 50 µM FAC-treated U-251 MG; 67.89 ± 2.95, p-value = 0.0038 for 100 µM FAC-treated U-251 MG, versus U-251 MG control: 100.00 ± 7.40, Fig. 1a).Vice versa, FAC did not alter T98-G cells metabolic activity at any tested concentrations and/or time-points (Fig. 1b). Moreover, we evaluated cytotoxicity effects of FAC on both cell lines via extracellular lactate dehydrogenase (LDH) assay, confirming that U-251 MG cells are more sensitive to ferroptosis induction, as compared to T98-G (Figure S1). To prove that cell death was not correlated to apoptosis, we performed an immunofluorescence staining for Cleaved Caspase-3 (Cl-Casp3). Our data showed that there were no differences between control and FAC-treated in both cell lines, demonstrating that cytotoxicity effect was not linked to Cl-Casp3-mediated cell death (Figure S1).

Similar outcomes for metabolic turnover were also observed after ferroptosis induction mediated by erastin, a ferroptosis activator. U-251 MG cells showed a decreased MTT turnover at 24 h (23.54 ± 2.10, p-value = 0.0074 for 20 µM erastin-treated U-251 MG at 24 h versus U-251 MG control at 24 h: 100.00 ± 7.42, Fig. 2a) and at 48 h (55.45 ± 7.37, p-value = 0.0288 for 2 µM erastin-treated U-251 MG at 48 h; 46.83 ± 7.89, p-value = 0.0079 for 5 µM erastin-treated U-251 MG at 48 h; 33.67 ± 1.26, p-value = 0.0010 for 10 µM erastin-treated U-251 MG at 48 h; 23.58 ± 1.20 for 20 µM, p-value = 0.0002 erastin-treated U-251 MG at 48 h versus U-251 MG control at 48 h:

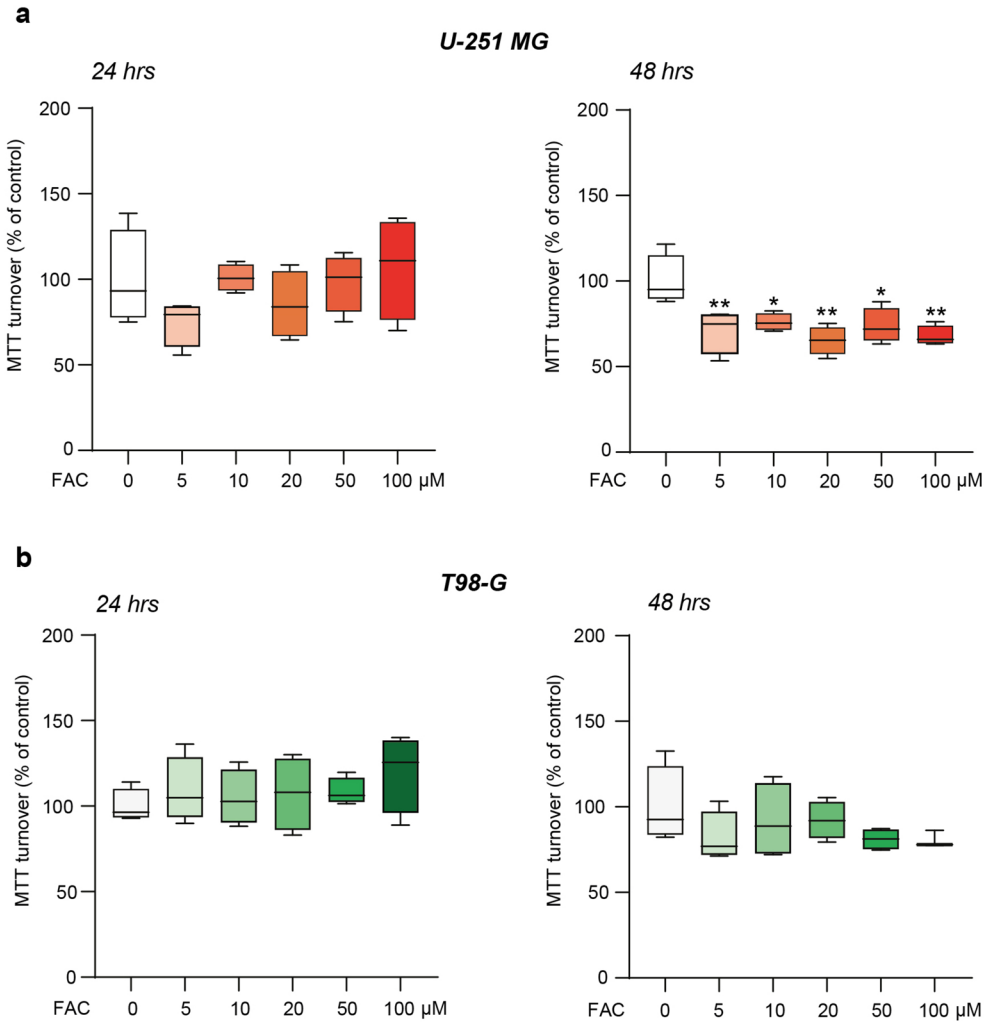

Fig. 1. Effect of FAC administration on MTT turnover on U-251 MG and T98-G cell lines. (**a**) MTT turnover on U-251 MG treated with 0, 5, 10, 20, 50, 100 µM of FAC at 24 and 48 h. (**b**) MTT turnover on T98-G treated with 0, 5, 10, 20, 50, 100 µM of FAC at 24 and 48 h. Data are shown via standard box and whiskers of $n \geq 3$ independent replicates for each experimental condition. *p-value < 0.05; **p-value < 0.01; versus 0 µM controls.

100.00 ± 16.36; Fig. 2a). On the other hand, T98-G cells did not show any significant change in MTT turnover upon erastin administration (Fig. 2b).

This evidence demonstrates that T98-G cells are more tolerant towards iron overload mediated by FAC and towards the ferroptosis inducer erastin as compared to U-251 MG cells.

Ferroptosis inducers prompt ROS accumulation in U-251 MG and T98-G cell lines

Since ferroptosis induction is related to ROS accumulation, we decided to quantify ROS levels by flow cytometry-assisted analysis, following 30, 90 and 180 min ferroptosis-inducers supplementation. We observed a significant increase of ROS production in U-251 MG cells as early as 30 min after FAC overload (Fig. 3a). Erastin was able to induce ROS accumulation in U-251 MG after 90 and 180 min post-treatment (Fig. 3a-b). Notably, T98-G cells also showed increased ROS levels after treatment, which became evident at 180 min (Fig. 3c, d). AUC quantification demonstrated that ROS overproduction after FAC and erastin administration occurred in both cell lines, demonstrating that T98-G tolerance toward ferroptosis was not related to a reduction of ROS accumulation.

T98-G cell line shows higher GSH levels as compared to U-251 MG cells

Given the superimposable oxidative response mediated by FAC and erastin treatment in U-251 MG and T98-G cells, we aimed at clarifying the underlying cellular mechanisms that sustain T98-G tolerance to ferroptosis.

We first tested the expression levels of CD71, a transmembrane glycoprotein involved in iron intake. Given the role of CD71 in determining cellular iron pool, this receptor could be considered a ferroptosis marker[31,32]. Thus, we performed western blot analysis to analyze CD71 levels in both cell lines, after FAC administration. We found that 100 µM of FAC was not able to significantly increase CD71 levels for both the CD71 protein bands at 90 kDa and for the bands at about 180 kDa, which is likely the receptor dimer, in U-251 MG and in T98-G

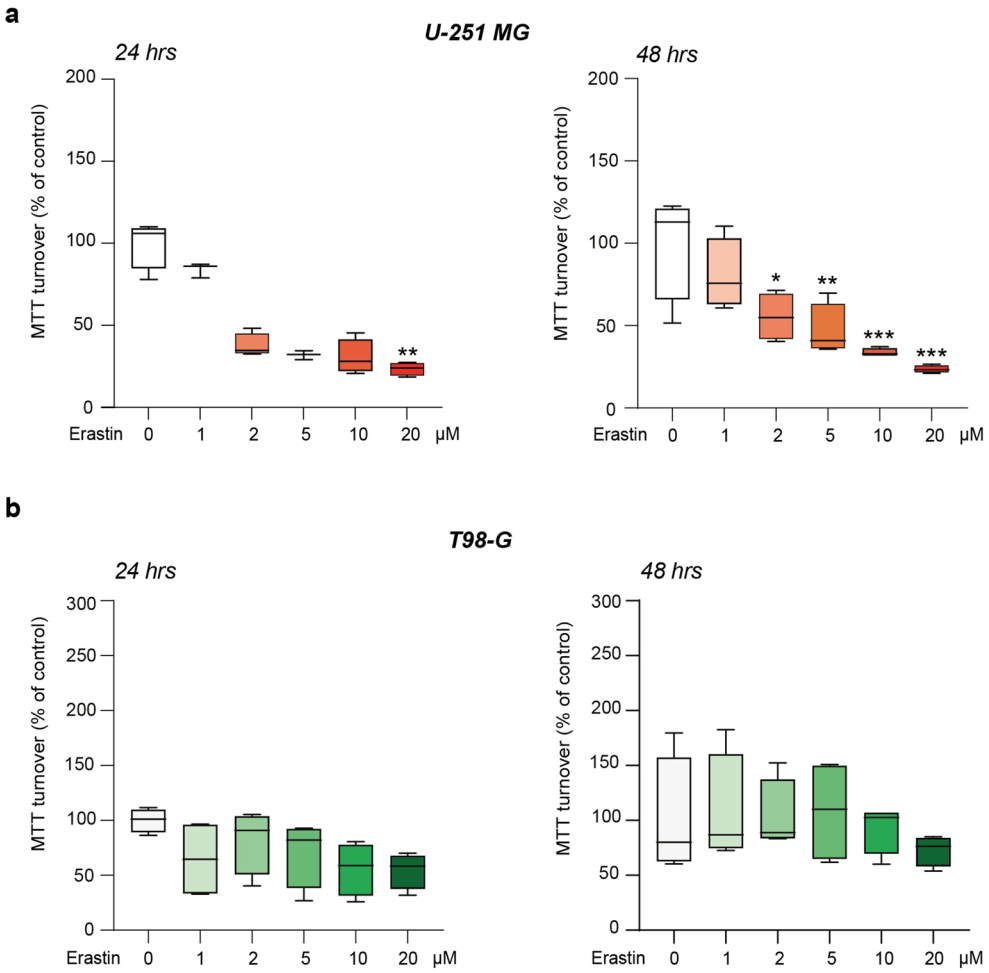

Fig. 2. MTT turnover on U-251 MG and T98-G cells after erastin administration. (**a**) MTT turnover on U-251 MG, 24 and 48 h post-erastin treatment at different concentrations (0, 1, 2, 5, 10, 20 μM). (**b**) MTT turnover on T98-G, 24 and 48 h post-erastin treatment at different concentrations (0, 1, 2, 5, 10, 20 μM). Data are shown via standard box and whiskers of $n \geq 3$ independent replicates for each experimental condition. *p-value < 0.05; **p-value < 0.01; ***p-value < 0.001 versus 0 μM controls.

cell lines, suggesting that the different tolerance mechanisms between the two cell lines were not related to iron internalization (Fig. 4a, b).

Next, through GSH quantification analysis, we investigated the antioxidant system of the two cell lines. We found that basal GSH levels were higher in T98-G cells as compared to U-251 MG (5.72 ± 0.12 nmol for U-251 MG vs. 7.43 ± 0.39 nmol for T98-G, p-value = 0.0141, Fig. 4c). Moreover, we performed a qRT-PCR for GPX4 mRNA expression levels on control and FAC treated cells. On the one hand, we found that T98-G expressed a significant up-regulation of GPX4 after FAC treatment of about 260 folds as compared to control. On the other hand, U-251 MG exhibited a slight not-significant reduction of GPX4 mRNA levels after FAC treatment (Fig. 4d). These findings support the hypothesis that T98-G cells had a better and more effective antioxidant system to resist to ferroptosis inducers.

Glioblastoma mesenchymal subtype up-regulates genes involved in antioxidant processes

In an effort to correlate ferroptosis resistance to proneural or mesenchymal GBM subtype, we analysed a publicly available dataset (GSE119637) on the most commonly used GBM cell lines[33].

To assign a subtype to U-251 MG and T98-G cells, we compared 7 different cell lines, namely T98-G, LN-18, U-138 MG, U-87 MG, A-172, LN-229 and U-251 MG, evaluating the expression of either proneural or mesenchymal subtype-related markers. Our analysis suggested that T98-G cells showed an up-regulation of mesenchymal-related markers, whereas U-251 MG cells exhibited an increased expression of proneural markers (Fig. 5a). To confirm this finding, we moved to analyse T98-G and U-251 MG phenotype using an independent database available on Cancer Cell Line Encyclopedia (CCLE) of Xena UCSC (Fig. 5b). Our analysis confirmed that T98-G cells express higher levels of all mesenchymal markers as compared to U-251 MG, while *SOX2, PDGFRA*, *DLL3* and *NCAM1* were found to be increased in terms of z-score in U-251 MG versus T98-G (Fig. 5b).

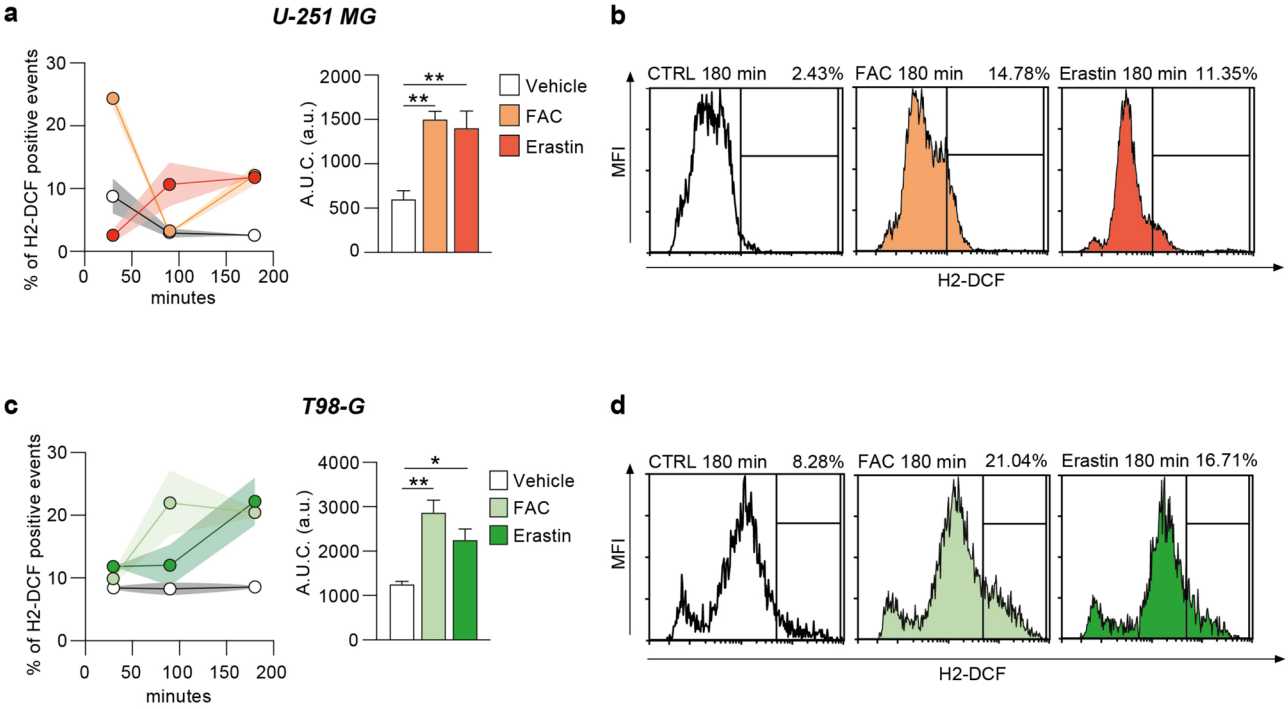

Fig. 3. ROS production in U-251 MG and T98-G cells after FAC and erastin administration. (**a**) Area under curve (AUC) quantification for % of H2-DCF positive events in U-251 MG, following 30, 90 and 180 min of FAC and erastin treatment. (**b**) Representative plots of ROS production at 180 min post-treatment in U-251 MG. (**c**) AUC quantification for % of H2-DCF positive events in T98-G, following 30, 90 and 180 min of FAC and erastin treatments. (**d**) Representative plots of ROS production at 180 min post-treatment in T98-G. Data are shown as mean ± SEM of n = 4 independent experiments. *p-value < 0.05; **p-value < 0.01.

In order to evaluate the expression of genes involved in ferroptosis in human GBM biopsies, we performed a bioinformatic analysis on a selected RNA-seq dataset from GBM biopsies of n = 9 proneural tumors and n = 14 mesenchymal tumors. We selected 209 genes involved in ferroptosis, which were divided into 3 groups, according to their role: i) iron mobility, ii) redox and iii) transmembrane (Fig. 6a). We identified 8 genes, *SLC48A1* and *TF*, related to iron mobility, *COQ3* and *QDPR*, related to redox, and *GRM1*, *KCNJ10*, *SLC1A1* and *SLC1A6* related to transmembrane signalling, which were down-regulated in mesenchymal-diagnosed GBM as compared to proneural-diagnosed GBM biopsies (Fig. 6b). Notably, most genes were significantly up-regulated in mesenchymal-diagnosed GBM as compared to proneural subtype and were related to redox mechanisms (Fig. 6c). Of note, we found that *GSS*, encoding for GSH, was up-regulated in mesenchymal tumors (4.90 ± 0.29 in mesenchymal vs 4.35 ± 0.44 in proneural, p-value = 0.0017; Fig. 6c), confirming that mesenchymal subtype better and more effectively responds to oxidative stimuli as compared to proneural subtype.

Iron mobility and redox signature genes correlate with reduced overall survival in GBM patients

To validate the prognostic potential of the identified genes, we analysed an independent dataset of GBM patients available on Xena UCSC (TCGA Glioblastoma). We first performed an analysis of the potential differences among patients in terms of OS and PFI analysing either mesenchymal markers (Fig. 7a) or proneural markers (Fig. 7b). Our analysis showed no significant differences in OS between high expressing mesenchymal markers versus low expressing mesenchymal markers GBM patients (Fig. 7a), whereas a significant reduction in PFI was observed in high expressing mesenchymal markers GBM patients (164 vs 232 PFI for high and low expressing patients, respectively, p-value = 0.0225, Fig. 7a). Analysing GBM patients dataset for proneural markers, we confirmed no significant differences in OS, while we found a significant reduction in PFI in low expressing proneural markers GBM patients (239 vs 157 PFI for high and low expressing patients, respectively, p-value = 0.0054, Fig. 7b). These data collectively indicate that PFI is significantly influenced by GBM subtypes, whether analysis of OS data did not highlight any significant correlation. We finally performed an OS and PFI analysis using the significant up-regulated genes identified as significantly up-regulated in mesenchymal subtypes and involved in iron mobility (Fig. 7c). Our data showed that high expressing mesenchymal iron mobility genes GBM patients were characterized by a significant reduction of OS and PFI (357 vs 455 OS for high and low expressing patients, respectively, p-value = 0.0308; 164 vs 311 PFI for high and low expressing patients, respectively, p-value = 0.0027; Fig. 7c). Importantly, we expanded over this evidence analysing the signature of significantly up-regulated genes in mesenchymal GBM involved in redox status. Our analysis revealed that high expressing redox genes GBM patients showed a significant OS and PFI reduction as compared to low expressing GBM patients (342 vs 454 OS for high and low expressing patients, respectively, p-value = 0.0082; 151 vs 308 PFI for high and low expressing

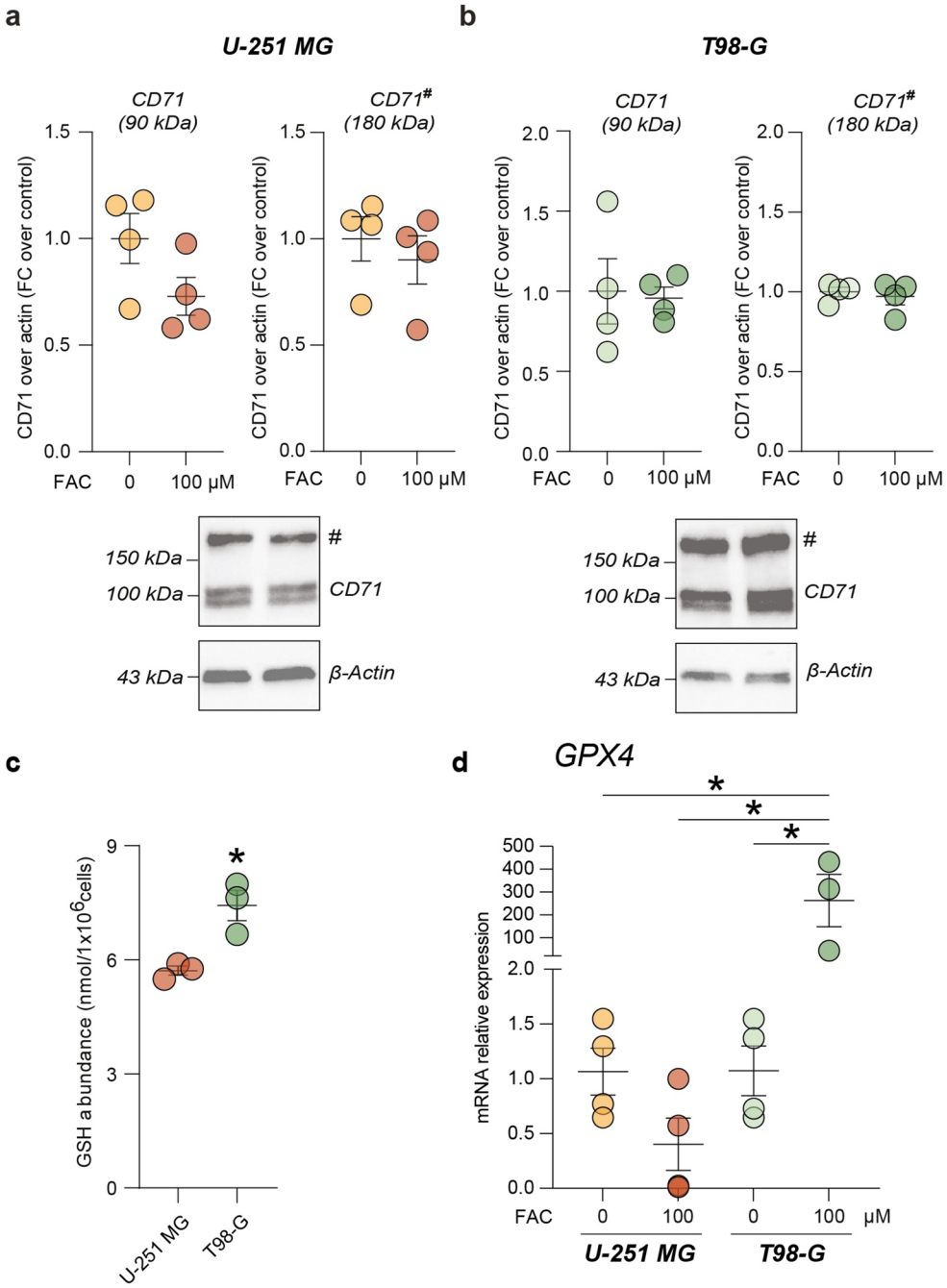

Fig. 4. Western blot for CD71, GSH levels analysis and mRNA expression levels of GPX4. (**a**) Quantification of western blot analysis of CD71 bands at 90 kDa and at about 180 kDa (labelled by #), and representative cropped blots on U-251 MG exposed to 0 or 100 µM of FAC. (**b**) Quantification of western blot analysis of CD71 bands at 90 kDa and at about 180 kDa (labelled by #), and representative cropped blots on T98-G exposed to 0 or 100 µM of FAC. Data are expressed as FC over control ± SEM of n = 4 independent experiments. Whole uncropped blots are presented in Figure S2. (**c**) GSH basal levels in U-251 MG and T98-G cells. Data are expressed as mean ± SEM of n = 3 independent experiments. *p-value < 0.05. (**d**) qRT-PCR analysis of mRNA expression levels of GPX4 in both U-251 MG and T98-G cell lines exposed to 0 or 100 µM of FAC. Data are expressed as mean ± SEM of n ≥ 3 independent experiments. *p-value < 0.05.

patients, respectively, p-value = 0.0013; Fig. 7d). These data uncover a significant prognostic value of mesenchymal markers coupled with iron mobility and/or redox signature genes for GBM patients.

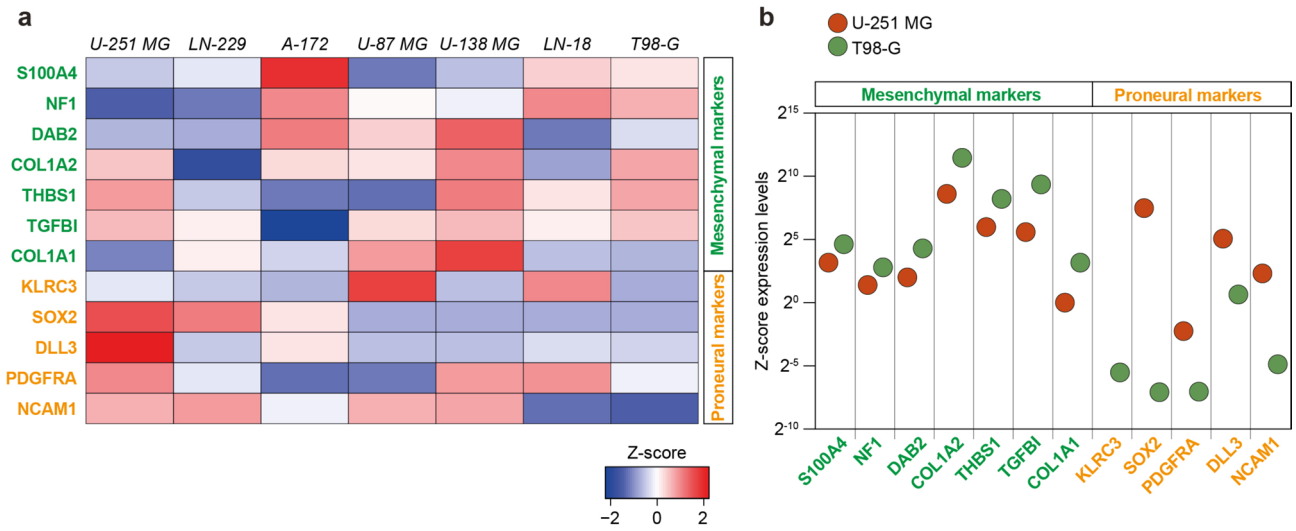

Fig. 5. U-251 MG and T98-G cells expression levels of proneural and mesenchymal markers. (**a**) Heatmap of Z-score values of selected signature markers of either mesenchymal or proneural GBM subtypes on 7 selected cell lines included in the dataset GSE119637. (**b**) Z-score expression levels of signature markers of either mesenchymal or proneural subtype for T98-G and U-251 MG cells included in Cancer Cell Line Encyclopedia (CCLE) of Xena UCSC.

Discussion

GBM is still characterized by a high mortality rate and it is one of the most aggressive and resistant tumors able to overcome radiotherapy- and chemotherapy-induced damages[34–36]. Given GBM cellular and molecular characteristics, new approaches are needed to evaluate its heterogeneity in a patient-specific manner to develop personalized therapies[37–39].

In the last years, it has been proven that ferroptosis could be considered a potential and effective anti-cancer approach, indeed ferroptosis inducers showed in vitro and in vivo efficacy, also demonstrating a beneficial synergism with chemotherapy drugs in certain cancer cells[40–42]. However, despite the potential of this strategy, some tumors overcome ferroptosis-related oxidative stress, showing resistance to ferroptosis-induced therapy[43,44]. The mechanisms underlying sensitivity or resistance to iron-dependent cell death are a growing area of research. Indeed, this process involves a number of proteins and intercellular factors that collectively contribute to the cell-specific sensitivity to this form of cell death[40,45].

Ferroptosis can be induced by different molecules, and among these, erastin is a ferroptosis activator acting on system xc – cystine/glutamate antiporter, to inhibit the SLC7A11 subunit and leading to the inactivation of GPX4, an antioxidant mediator that decreases membrane phospholipid hydroperoxides[15,46–48]. An alternative approach to trigger ferroptosis is to induce intracellular iron overload by ferric citrate, that increases Fe^{2+} levels, leading to ROS accumulation and lipid peroxidation[49–51].

Our aim was to investigate the effects of FAC and erastin on 2 different GBM cell lines, U-251 MG and T98-G, examining their response to ferroptosis inducers. We evaluated the effects of FAC on cellular metabolic turnover, showing that FAC and erastin were able to reduce metabolic turnover in U-251 MG cells, whereas T98-G cells did not show any significant change at any tested time-points, either with FAC or with erastin. These results demonstrate a different sensitivity to ferroptosis between GBM cell lines.

Subsequently, we observed that a typically cell response to FAC- or erastin-mediated ferroptosis was the increased levels of ROS. Notably, oxidative stress was observed in both sensitive- and resistant-ferroptosis cells. Thus, we studied molecular players of iron and antioxidant system to identify candidate genes involved in T98-G ferroptotic resistance. Among them, CD71, also known as type I transferrin receptor (TfR1), is a transmembrane glycoprotein engaged in iron internalization[52,53]. CD71 fosters the uptake of cellular iron, thus it can be considered a principal contributor to ferroptosis[31,47]. We examined whether the resistance of T98-G cells to FAC was associated with a change in CD71 expression and, consequently, to an altered iron internalization. We observed that T98-G cells did not modulate CD71 expression after FAC treatment, thus resistance mechanisms were not related to CD71 and iron uptake.

Multiple metabolic processes may affect cells susceptibility to ferroptosis, which is regulated by 3 different antioxidant axes: (i) system xc – /GSH/GPX4 axis, (ii) ferroptosis suppressor protein 1/Coenzyme Q10 (FSP1/CoQ10) axis and (iii) GTP cyclohydrolase I/Tetrahydrobiopterin/Dihydrofolate reductase (GCH1/BH4/DHFR) axis[17].

Among them, GPX4 axis depends on GSH oxidative state. It represents one of the most important regulators of cellular oxidative homeostasis, and it is the principal substrate for GPX4, therefore, a reduced GSH activity can impact GPX4 stability, increasing ferroptosis susceptibility[54]. Moreover, the system xc – cystine/glutamate antiporter and transsulfuration pathway, supplying cysteine, are also involved in cyst(e)ine/GSH/GPX4 axis[55]. FSP1/CoQ10 axis, on the other hand, involves mevalonate pathway, which produces CoQ10. In particular, FSP1 prevents lipid autoxidation through CoQ10, regulating ferroptosis[56]. Whereas GCH1 seems to be able to block

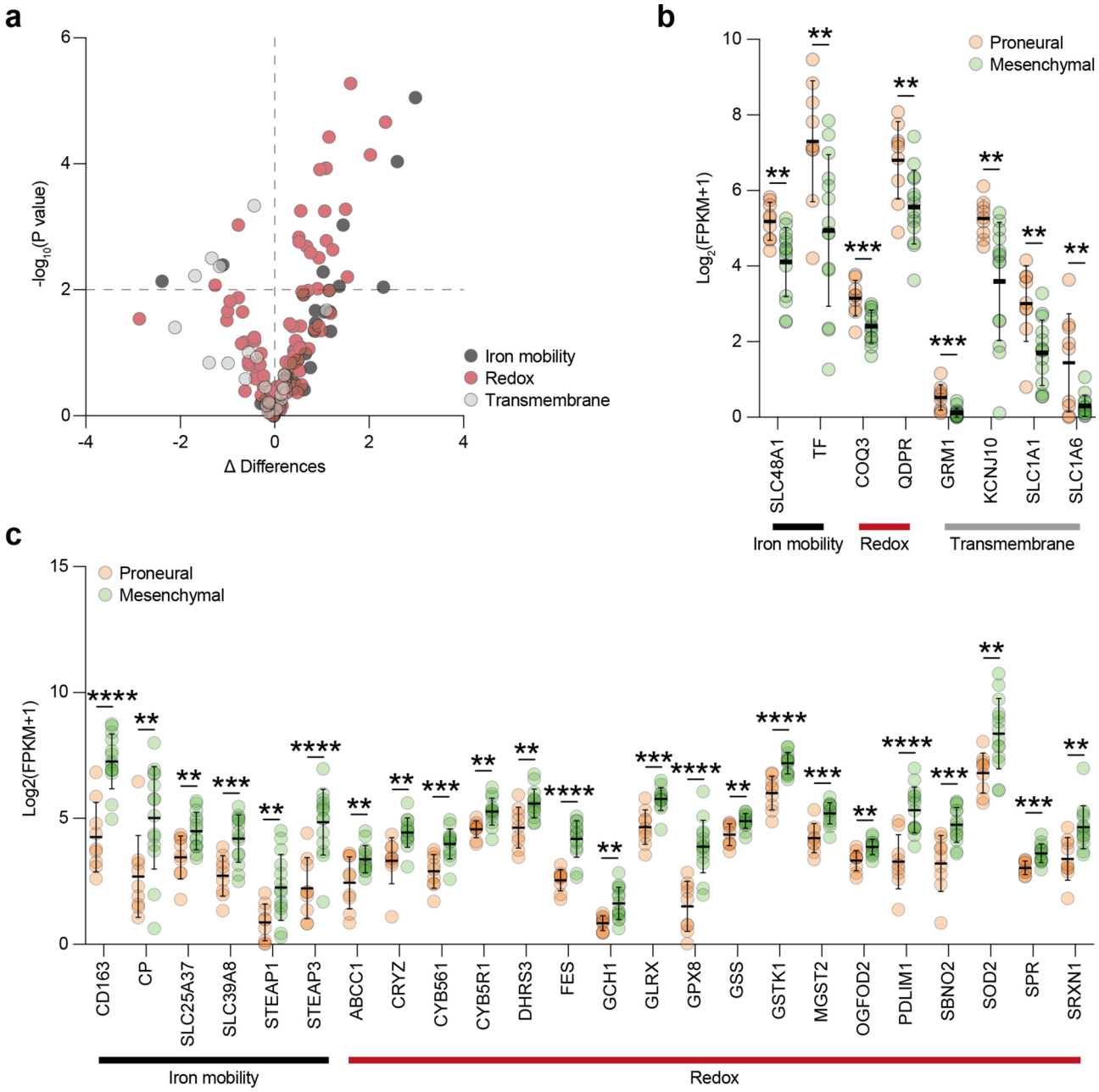

Fig. 6. Bioinformatic analysis on RNA-seq dataset of human GBM biopsies. (**a**) Volcano plot of selected 209 genes, divided into three groups. (**b**) Genes down-regulated in mesenchymal tumors as compared to proneural ones. (**c**) Genes up-regulated in mesenchymal tumors as compared to proneural ones. Data are expressed as mean ± SD and aligned dot plot. **p-value < 0.01; ***p-value < 0.001 and ****p-value < 0.0001.

ferroptosis in a GPX4-independent manner, involving BH4, a lipophilic radical-trapping antioxidant[57]. Thus, we further investigated antioxidant mechanisms through GSH quantification and GPX4 mRNA expression analysis. From our data, it was evident that GSH basal levels were higher in T98-G as compared to U-251 MG cells and that mesenchymal cells are able to up-regulate GPX4 after FAC treatment, reducing ferroptosis inducers efficacy. Then, to correlate the different response of GBM cell lines with GBM heterogeneity, we assessed the similarities between U-251 MG and T98-G cell profile and GBM phenotype. By analysing a publicly available dataset on 7 GBM cell lines, we evaluated the expression of genes characterizing mesenchymal or proneural subtype. This assessment revealed that T98-G showed a mesenchymal phenotype as opposed to U-251 MG with a proneural profile. Furthermore, we took advantage of RNA-seq data from biopsies of GBM patients, grouped according to their subtype. Based on these analyses, we observed that mesenchymal GBM patients showed a better antioxidant profile, which makes them more resistant to therapy and, particularly, to ferroptosis-based approaches.

The increased expression of GSS mRNA, encoding for GSH, in GBM mesenchymal subtypes as compared to proneural ones, supports the hypothesis of a more effective antioxidant system xc−/GSH/GPX4 axis. Indeed, GSH metabolism and its antioxidant mechanism are among the major regulators of ferroptosis sensitivity[40].

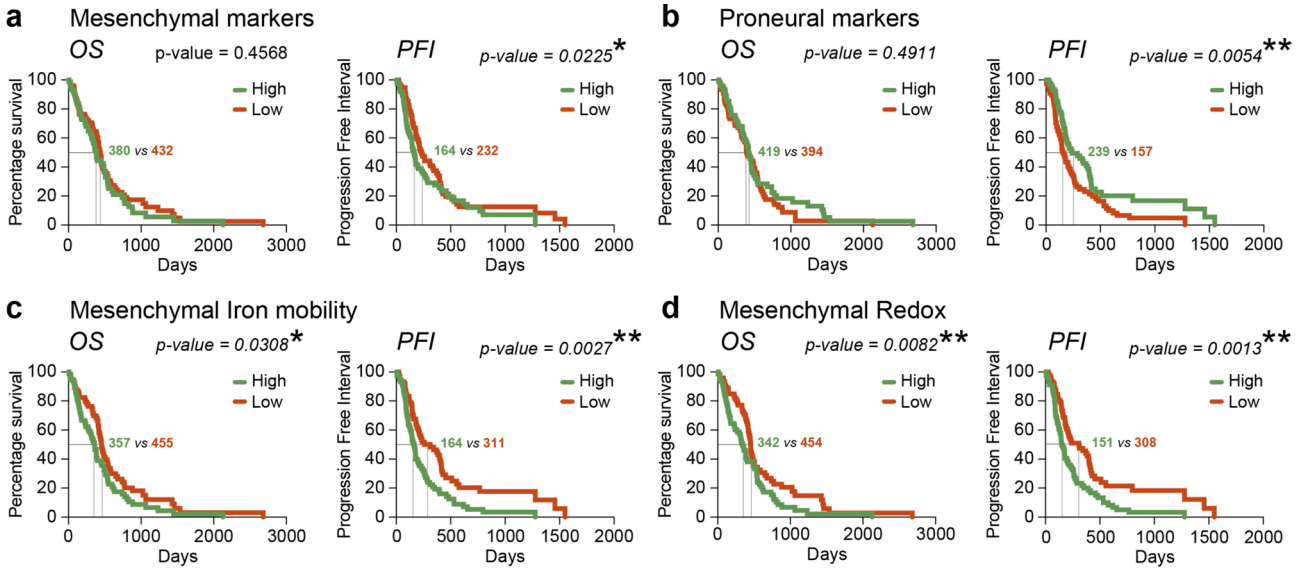

Fig. 7. Overall survival (OS) and Progression Free Interval (PFI) analysis of GBM patients. (**a–d**) Kaplan Meier plot of OS and PFI of GBM patients selected for high versus low expression of mesenchymal markers (cut-off value = 73.57) (**a**), proneural markers (cut-off value = 50.27) (**b**), mesenchymal iron mobility (cut-off value = 54.83) (**c**) and mesenchymal redox (cut-off value = 170.4) (**d**). *p-value < 0.05; **p-value < 0.01.

After uptake by system xc−, cystine is catalysed to GSH and GPX4 transforms GSH to GSSH, decreasing lipid peroxidation and inhibiting ferroptosis[58]. Moreover, mesenchymal tumors also exhibited an increased expression of *GCH1* gene, within the GCH1/BH4/DHFR axis, which is an antioxidant axis involved in ferroptosis susceptibility, again supporting an increased defensive response as compared to the proneural tumors.

We also observed that combination of mesenchymal and iron mobility markers or mesenchymal and redox markers showed a significant impact on OS and PFI of GBM patients. This evidence is of critical importance, considering that the OS analysis of GBM patients expressing mesenchymal or proneural markers failed to reveal differences in terms of OS. Therefore, our data emphasize that GBM heterogeneity is a highly significant aspect to be considered in therapy, and that current GBM classification is of critical importance to establish personalized approaches. More detailed studies on mechanistic processes are needed to identify potential targets to overcome ferroptosis resistance and counteract aggressive cancers such as GBM.

Although we were able to stratify commonly used GBM cell lines, this study has potential limitations that need to be addressed in future research. Indeed, an in-depth analysis of the fundamental biological mechanisms underlying ferroptosis resistance on additional mesenchymal or proneural GBM cell lines is required. Additionally, given the characteristics of mesenchymal, proneural and classical GBM subtypes, expanding this analysis on patient-derived cell lines would increase the impact and significance of the findings herein described and also will offer significant insights in clarifying these mechanisms.

In conclusion, our data suggest that GBM subtypes differently tolerate ferroptosis inducers. Proneural subtypes reduced their metabolic turnover after FAC or erastin administration, on the contrary mesenchymal subtype did not exhibit significant alterations. GSH upregulation in mesenchymal GBM cells could be involved in these mechanisms by mitigating the effects of ferroptosis inducers and hampering cell death. Moreover, RNA-seq dataset of GBM patients revealed a better antioxidant profile in mesenchymal as compared to proneural tumors, demonstrating that ferroptosis might constitute a promising treatment option for proneural subtypes, but likely ineffective for mesenchymal. Given GBM heterogeneity, it is needed to investigate molecular aspects of specific subtypes in order to achieve a targeted and personalized therapy for each patient.

Methods

Cell Lines and drugs administration

Experiments were performed using U-251 MG (RRID: CVCL_0021) and T98-G (RRID: CVCL_0556) human GBM cell lines. Cells were purchased from European Collection of Authenticated Cell Cultures (ECACC, Public Health England). U-251 MG and T98-G were cultured in Dulbecco's Modified Eagle Medium (DMEM) High glucose (Cat# 11965092, Gibco) supplemented with 10% Foetal Serum Bovine (FBS, Cat#26140079, Gibco), 100 IU/mL Penicillin–Streptomycin solution (pen-strep, Cat#15140-122, Gibco) and 1 mmol/L sodium pyruvate (Cat#11360-039, Gibco). Cells were maintained in an incubator at 37 °C in a humidified atmosphere (95% air and 5% CO_2) and were routinely sub-cultured in standard culture flasks. FAC (Cat#A11199.30, Alfa Aesar-Thermofisher) was prepared as a 50 mM stock solution in phosphate-buffered saline (PBS) and used at reported working concentrations (i.e., 5, 10, 20, 50, 100 µM). Erastin (Cat#S7242, Selleckchem) was dissolved at 2 mM in dimethyl sulfoxide (DMSO) (Cat#P60-36720100, Pan-biotech) for the stock solution and was used at described final concentrations (i.e., 1, 2, 5, 10, 20 µM).

Cell doubling time

U-251 MG and T98-G were seeded in T-25 flasks at a final concentration of 25×10^4 cells/flask and cultured at 37 °C in a humidified 5% CO_2 incubator. On the third day, when cells reached about the 90% of confluency, U-251 MG and T98-G were detached with Trypsin–EDTA 0.25% (Cat#25200-056, Gibco) and counted using a cell counter. Cell doubling time was calculated following equation:

$$Cell\ Doubling\ Time = \frac{[T * (ln2)]}{[ln(\frac{Xe}{Xb})]}$$

where T is cell culture time in days, Xb is the initial number of cells and Xe is the final number of cells.

Metabolic turnover assay

To evaluate U-251 MG and T98-G cells metabolic turnover, 3-(4,5-dimethylthiazol-2-yl)-2,5-diphenyltetrazolium bromide (MTT, Cat#M5655, Sigma-Aldrich) assay was performed. Cells were seeded in 96-well plates at a final density of 1×10^4 cells/well/100 µL and incubated for 24 h. After, cells were exposed to different FAC concentrations, from 5 to 100 µM, or erastin, from 1 to 20 µM, and incubated for 24 or 48 h. MTT at a final concentration of 1 mg/mL was added to each well and incubated under standard culture conditions. After 2.5 h, media were removed, 200 µL of DMSO (Cat#P60-36720100, Pan-biotech) was added, and plates were shacked on an orbital shaker for 10 min at room temperature. The absorbance was measured using a Multiskan SkyHigh Microplate spectrophotometer (Thermo Scientific) at 570 nm. Metabolic turnover was calculated as: (optical density sample/average optical density control) × 100. Results were expressed as the percentage of MTT turnover versus control.

LDH assay

The relative cytotoxicity was assessed using LDH activity assay (Cat#CBA-241, Cell Biolabs, Inc.), following the manufacturer's instructions. Briefly, cells were seeded in 96-well plates at a final density of 1×10^4 cells/well/200 µL, then, exposed to 100 µM FAC, and incubated for 6 h. Cells treated with 1% of lysis solution (Triton X-100 Solution, Cat#124102, Cell Biolabs, Inc.) were used as positive controls (i.e. 100% relative cytotoxicity). Vehicle-treated cells were used as negative control (i.e. 0% relative cytotoxicity). Quantification of the LDH activity was performed on supernatants following manufacturer's instructions. The absorbance was measured using a Multiskan SkyHigh Micro-plate spectrophotometer (Thermo Scientific) at 450 nm. The percentage of relative cytotoxicity was calculated using the following formula:

$$\%relative\ cytotoxicity = \left[\frac{(ODsample - ODnegative\ control)}{(ODpositive\ control - ODnegative\ control)}\right] * 100$$

Immunofluorescence

For immunofluorescence staining, cells were seeded on 24-well plate, using 12 mm coverslips, at a final density of 1×10^5 cells/well and incubated at 37 °C, 5% CO_2 for 12 h. Then, 100 µM FAC was added on cells and maintained for 24 h. On the following day, cells were fixed using 4% paraformaldehyde (PFA) and permeabilized in 0.1% Triton X100 in PBS. Samples were incubated with blocking solution (10% normal goat serum, NGS in 0.1% Triton X100 in PBS) for 1 h at room temperature. Then, cells were incubated overnight at 4 °C with the primary antibody (1:300, Rabbit anti-Cl Casp3, Cat#9661, RRID: AB_2341188, Cell Signalling) diluted in incubating solution (1% NGS in 0.1% Triton X100 in PBS). The day after, sample were washed with 0.1% Triton X100 in PBS and incubated for 1 h at room temperature with the appropriate fluorescent secondary antibody (1:1000, Alexa Fluor goat anti-rabbit 546, Cat# A11010, RRID: AB_143156, Invitrogen) diluted in incubating solution. Following 3 washes with 0.1% Triton X100 in PBS, F-actin was stained with Alexa Fluor 488 Phalloidin (1:300, Cat#A12379, Invitrogen). Samples were washed again, and nuclei were counterstained with 4′,6-diamidino-2-phenylindole (DAPI, 1:1000, Cat# D1306, Invitrogen) for 3 min at room temperature. Cover slips were then mounted with Fluoromount™ Aqueous Mounting Medium (Sigma-Aldrich, Cat#F4680). Digital images were acquired using a Leica TCS SP8 confocal microscope. Quantification of the percentage of positive cells was obtained by quantifying the number of Cl Casp3-positive cells over total DAPI-positive cells from $n \geq 3$ randomized regions of interest (ROI) per group.

Flow cytometry

For flow cytometry-assisted viability analysis, 5×10^4 cells were plated in 24-well plates. The next day, cells were respectively treated with: vehicle, 100 µM FAC or 10 µM erastin. After 30, 90 or 180 min, cells were collected and resuspended in 500 µl of PBS. ROS were detected using 2',7'-dichlorodihydrofluorescein acetate (H2-DCF; Cat# D399, Sigma-Aldrich), and fluorescence intensity was measured according to the fluorescence detection conditions of fluorescein isothiocyanate (FITC) using a MACSQuant Analyzer (Miltenyi Biotech).

Western blot

For western blot analysis, cells were seeded in 6-well plates at a final density of 5×10^5/well and incubated at 37 °C. The next day, 100 µM FAC was added on cells and maintained for 24 h. Then, cells were collected to obtain a dry pellet. Proteins were extracted using RIPA Lysis Buffer (50 µL/sample; Cat#ab156034, Abcam) supplemented with protease inhibitor (1:100, Cat#P8340, Merck). Samples were incubated for 20 min at room temperature and centrifuged at 13,000×*g* for 3 min. 50 µg of proteins were electrophoresed on 4–15% Mini-PROTEAN TGX

gels (Cat#4561083, Bio-Rad) and transferred to 0.2 µm nitrocellulose membranes of Trans-Blot Turbo Transfer Pack (Cat#1704158, Bio-Rad), using Trans-Blot Turbo Transfer System (Bio-Rad). Membranes were incubated for 1 h at room temperature with blocking buffer (5% non-fat milk in 0.1% tween-20 in PBS) and then overnight at 4 °C with primary antibodies diluted in blocking buffer. The primary antibodies, mouse anti-CD71 (1:1000, Cat#13-6800, RRID: AB_2533029, Invitrogen) and mouse β-actin (1:1000, Cat#sc-47778, RRID: AB_626632, Santa Cruz Biotechnology), were used for western blot. The day after, membranes were washed 3 times in 0.1% tween-20 in PBS and then incubated for 1 h at room temperature with the corresponding secondary antibody: Goat anti-Mouse IgG (H + L) Secondary Antibody, HRP (1:5000, Cat#31430, AB_228307, Invitrogen). Proteins bands were visualized with a ChemiDoc System (Bio-Rad) and protein levels were quantified by densitometric analysis. ImageJ analysis software was used to quantify the density of each band, that then was normalized to the β-actin optical density measured in the same membrane. All values are shown as the mean fold change (FC) over control ± SEM.

qRT-PCR

Gene expression on U-251 MG and T98-G was tested by performing qRT-PCR. Cell pellets were resuspended in TRIzol (Cat#15596018, Thermo Fisher Scientific). RNA extraction was performed by chemical separation as previously described[59]. cDNA was obtained by using High-Capacity cDNA Reverse Transcription Kit (Cat#4368814, Thermo Fisher Scientific) according to manufacturer's protocol. Gene expression was analyzed using PowerUp™ SYBR™ Green Master Mix for (Cat#A25741, Thermo Fisher Scientific) and Rotor-Gene Q 2plex (Qiagen). The relative expression level was determined by comparison with the control housekeeping ribosomal RNA 18S by using the 2^ – ΔΔCt method. Primers used for this assay are reported in Table 1.

Cell deproteinization and HPLC analysis of GSH

Cells were plated in T-75 flasks. After 24 h, cells (1×10^6 cells/ml) were trypsinized, resuspended in ice-cold PBS and centrifuged at 1860×*g*. Following a well-established method[60], cellular pellet was deproteinized in a precipitating solution (75% acetonitrile + 25% KH_2PO_4 10 mM pH 7.4) and centrifuged at a high speed (20,890×*g* for 10 min at 4 °C). Subsequently, supernatant was supplemented with double volume of chloroform to definitively obtain the aqueous phase. Separation of GSH was obtained flowing samples throughout a C18 chromatographic column (Hypersil C-18, 250 × 4.6 mm, 5 µm particle size) settled in a HPLC apparatus (ThermoFisher Scientific, Spectra System P4000 pump), whereas the diode array detector UV6000- tuned at 206 nm, was used for quantification and identification of the tripeptide[61,62].

Human GBM datasets selection and analysis

Gene Expression Omnibus (GEO) database (http://www.ncbi.nlm.nih.gov/geo/, accessed on 29 February 2024) was used to select RNA-seq datasets of interest. We chose two different datasets. The first one GSE119637 is based on 7 human GBM cell lines and expression data were collected for mesenchymal markers signature genes (i.e. *S100A4, NF1, DAB2, COL1A2, THBS1, TGFBI, COL1A1*) and for proneural markers signature genes (i.e. *KLRC3, SOX2, PDGFRA, DLL3, NCAM1*) for both cell lines (Table S1)[33]. The second dataset GSE145645 was selected to analyse transcriptome of human GBM biopsies[63]. A total of 34 GBM patients' biopsies were analysed and the following criteria were applied to select patients: i) patients diagnosed for mesenchymal or proneural GBM were included and ii) patients with not available GBM subtypes or classical GBM subtypes were excluded. A total of 23 GBM patients, divided into 14 GBM with mesenchymal subtype and 9 GBM with proneural subtype, were included within the present study (details are reported in Table S2). Finally, data on genes expression levels were obtained selecting 209 genes divided in 3 main gene signatures accordingly to previously published papers: iron mobility[64], redox[65–67] and transmembrane[67] processes (Table S3).

Gene expression profiles for human GBM cell lines were obtained from Cancer Cell Line Encyclopedia (CCLE) using Xena Browser (https://xenabrowser.net/, accessed on 29 February 2024)[68]. The following cell lines were selected from the cohort of cell lines: U-251 MG and T98-G. Expression data were collected for mesenchymal markers signature genes (i.e. *S100A4, NF1, DAB2, COL1A2, THBS1, TGFBI, COL1A1*) and for proneural markers signature genes (i.e. *KLRC3, SOX2, PDGFRA, DLL3, NCAM1*) for both cell lines (Table S1).

For Kaplan Meier Plots, data were obtained from GDC TCGA Glioblastoma (GBM) using Xena Browser (https://xenabrowser.net/, accessed on 29 February 2024)[68]. We selected primary tumors excluding from the subsequent analysis recurrent tumors, solid tissue normal and patients with null value of selected genes, obtaining a total of n = 153 patients. The cohort of GBM patients was divided in 2 groups automatically by Xena Browser into high and low, accordingly to the expression levels of either mesenchymal markers, proneural markers, mesenchymal and iron mobility markers or mesenchymal and redox markers (see Table S1, Table S3 and Table S4). The cut-off value was calculated as the median of the sum of values for the selected genes signature.

Gene	Forward primer	Reverse primer
GPX4	GCGGAAGGCCCCAGC	CACACGAAGCCCCGGTA
18S	CTTAGAGGGACAAGTGGCG	ACGCTGAGCCAGTCAGTGTA

Table 1. List of primers used for qRT-PCR.

Statistical analysis

Data analysis was performed using GraphPad Prism software version 8.0.1. A two-tailed unpaired Student's t-test was used for comparison of $n = 2$ groups. For Kaplan Meier analysis, curve comparison was analysed by Gehan-Breslow-Wilcoxon test for statistical significance. Moreover, median overall survival (OS) and progression free interval (PFI) were calculated for each group. For comparison of $n \geq 3$ groups, one-way analysis of variance (ANOVA) was used, followed by Holm-Sidak post-hoc test for multiple comparisons. Data are presented as the mean ± SEM (unless otherwise stated). $p < 0.05$ was considered statistically significant and symbols, used to indicate statistical differences, are represented in the figure legends.

Data availability

The datasets used and/or analyzed during the current study are available from the corresponding author on reasonable request.

Received: 23 April 2024; Accepted: 3 September 2024
Published online: 05 September 2024

References

1. Wirsching, H. G., Galanis, E. & Weller, M. Glioblastoma. *Handb. Clin. Neurol.* **134**, 381–397. https://doi.org/10.1016/B978-0-12-802997-8.00023-2 (2016).
2. Torrisi, F. *et al.* Epigenetics and metabolism reprogramming interplay into glioblastoma: Novel insights on immunosuppressive mechanisms. *Antioxidants* **12**, 220. https://doi.org/10.3390/antiox12020220 (2023).
3. Wen, P. Y. *et al.* Glioblastoma in adults: A Society for Neuro-Oncology (SNO) and European Society of Neuro-Oncology (EANO) consensus review on current management and future directions. *Neuro Oncol.* **22**, 1073–1113. https://doi.org/10.1093/neuonc/noaa106 (2020).
4. Fabro, F., Lamfers, M. L. M. & Leenstra, S. Advancements, challenges, and future directions in tackling glioblastoma resistance to small kinase inhibitors. *Cancers* **14**, 600. https://doi.org/10.3390/cancers14030600 (2022).
5. Torrisi, F. *et al.* The hallmarks of glioblastoma: Heterogeneity, intercellular crosstalk and molecular signature of invasiveness and progression. *Biomedicines* **10**, 806. https://doi.org/10.3390/biomedicines10040806 (2022).
6. Sottoriva, A. *et al.* Intratumor heterogeneity in human glioblastoma reflects cancer evolutionary dynamics. *Proc. Natl. Acad. Sci. U.S.A.* **110**, 4009–4014. https://doi.org/10.1073/pnas.1219747110 (2013).
7. Verhaak, R. G. *et al.* Integrated genomic analysis identifies clinically relevant subtypes of glioblastoma characterized by abnormalities in PDGFRA, IDH1, EGFR, and NF1. *Cancer Cell* **17**, 98–110. https://doi.org/10.1016/j.ccr.2009.12.020 (2010).
8. Azam, Z., To, S. T. & Tannous, B. A. Mesenchymal transformation: The Rosetta stone of glioblastoma pathogenesis and therapy resistance. *Adv. Sci.* **7**, 2002015. https://doi.org/10.1002/advs.202002015 (2020).
9. Bhat, K. P. L. *et al.* Mesenchymal differentiation mediated by NF-kappaB promotes radiation resistance in glioblastoma. *Cancer Cell* **24**, 331–346. https://doi.org/10.1016/j.ccr.2013.08.001 (2013).
10. Segerman, A. *et al.* Clonal variation in drug and radiation response among glioma-initiating cells is linked to proneural-mesenchymal transition. *Cell Rep.* **17**, 2994–3009. https://doi.org/10.1016/j.celrep.2016.11.056 (2016).
11. Chen, J. *et al.* A restricted cell population propagates glioblastoma growth after chemotherapy. *Nature* **488**, 522–526. https://doi.org/10.1038/nature11287 (2012).
12. Mowforth, O. D. *et al.* Personalised therapeutic approaches to glioblastoma: A systematic review. *Front. Med.* **10**, 1166104. https://doi.org/10.3389/fmed.2023.1166104 (2023).
13. Torrisi, F. *et al.* Connexin 43 and sonic hedgehog pathway interplay in glioblastoma cell proliferation and migration. *Biology* **10**, 767. https://doi.org/10.3390/biology10080767 (2021).
14. Bernstock, J. D. *et al.* A novel in situ multiplex immunofluorescence panel for the assessment of tumor immunopathology and response to virotherapy in pediatric glioblastoma reveals a role for checkpoint protein inhibition. *Oncoimmunology* **8**, e1678921. https://doi.org/10.1080/2162402X.2019.1678921 (2019).
15. Dixon, S. J. *et al.* Ferroptosis: An iron-dependent form of nonapoptotic cell death. *Cell* **149**, 1060–1072. https://doi.org/10.1016/j.cell.2012.03.042 (2012).
16. Jiang, X., Stockwell, B. R. & Conrad, M. Ferroptosis: Mechanisms, biology and role in disease. *Nat. Rev. Mol. Cell Biol.* **22**, 266–282. https://doi.org/10.1038/s41580-020-00324-8 (2021).
17. Zheng, J. & Conrad, M. The metabolic underpinnings of ferroptosis. *Cell Metab* **32**, 920–937. https://doi.org/10.1016/j.cmet.2020.10.011 (2020).
18. Carota, G. *et al.* Neuroprotective role of alpha-lipoic acid in iron-overload-mediated toxicity and inflammation in in vitro and in vivo models. *Antioxidants* **11**, 1596. https://doi.org/10.3390/antiox11081596 (2022).
19. Friedmann Angeli, J. P. *et al.* Inactivation of the ferroptosis regulator Gpx4 triggers acute renal failure in mice. *Nat. Cell Biol.* **16**, 1180–1191. https://doi.org/10.1038/ncb3064 (2014).
20. Zhang, C., Liu, X., Jin, S., Chen, Y. & Guo, R. Ferroptosis in cancer therapy: A novel approach to reversing drug resistance. *Mol. Cancer* **21**, 47. https://doi.org/10.1186/s12943-022-01530-y (2022).
21. Lei, G., Zhuang, L. & Gan, B. Targeting ferroptosis as a vulnerability in cancer. *Nat. Rev. Cancer* **22**, 381–396. https://doi.org/10.1038/s41568-022-00459-0 (2022).
22. Liang, C., Zhang, X., Yang, M. & Dong, X. Recent progress in ferroptosis inducers for cancer therapy. *Adv. Mater.* **31**, e1904197. https://doi.org/10.1002/adma.201904197 (2019).
23. Rao, G. M., Rao, A. V., Raja, A., Rao, S. & Rao, A. Role of antioxidant enzymes in brain tumours. *Clin. Chim. Acta* **296**, 203–212. https://doi.org/10.1016/s0009-8981(00)00219-9 (2000).
24. Lu, Q. *et al.* Recent advances in ferroptosis and therapeutic strategies for glioblastoma. *Front. Mol. Biosci.* **9**, 1068437. https://doi.org/10.3389/fmolb.2022.1068437 (2022).
25. Mitre, A. O. *et al.* Ferroptosis involvement in glioblastoma treatment. *Medicina* **58**, 319. https://doi.org/10.3390/medicina58020319 (2022).
26. Yang, W. S. *et al.* Regulation of ferroptotic cancer cell death by GPX4. *Cell* **156**, 317–331. https://doi.org/10.1016/j.cell.2013.12.010 (2014).
27. Zhuo, S. *et al.* Emerging role of ferroptosis in glioblastoma: Therapeutic opportunities and challenges. *Front. Mol. Biosci.* **9**, 974156. https://doi.org/10.3389/fmolb.2022.974156 (2022).
28. Drijvers, J. M. *et al.* Pharmacologic screening identifies metabolic vulnerabilities of CD8(+) T cells. *Cancer Immunol. Res.* **9**, 184–199. https://doi.org/10.1158/2326-6066.CIR-20-0384 (2021).
29. Kapralov, A. A. *et al.* Redox lipid reprogramming commands susceptibility of macrophages and microglia to ferroptotic death. *Nat. Chem. Biol.* **16**, 278–290. https://doi.org/10.1038/s41589-019-0462-8 (2020).

30. Brown, C. W., Chhoy, P., Mukhopadhyay, D., Karner, E. R. & Mercurio, A. M. Targeting prominin2 transcription to overcome ferroptosis resistance in cancer. *EMBO Mol. Med.* **13**, e13792. https://doi.org/10.15252/emmm.202013792 (2021).
31. Feng, H. *et al.* Transferrin receptor is a specific ferroptosis marker. *Cell Rep.* **30**, 3411-3423.e7. https://doi.org/10.1016/j.celrep.2020.02.049 (2020).
32. D'Aprile, S. *et al.* Anaplastic thyroid cancer cells reduce CD71 levels to increase iron overload tolerance. *J. Transl. Med.* **21**, 780. https://doi.org/10.1186/s12967-023-04664-9 (2023).
33. Schnoller, L. E. *et al.* Systematic in vitro analysis of therapy resistance in glioblastoma cell lines by integration of clonogenic survival data with multi-level molecular data. *Radiat. Oncol.* **18**, 51. https://doi.org/10.1186/s13014-023-02241-4 (2023).
34. Fox, B. M. *et al.* SUMOylation in glioblastoma: A novel therapeutic target. *Int. J. Mol. Sci.* **20**, 1853. https://doi.org/10.3390/ijms20081853 (2019).
35. Longhitano, L. *et al.* Lactate induces the expressions of MCT1 and HCAR1 to promote tumor growth and progression in glioblastoma. *Front. Oncol.* **12**, 871798. https://doi.org/10.3389/fonc.2022.871798 (2022).
36. Ou, A., Yung, W. K. A. & Majd, N. Molecular mechanisms of treatment resistance in glioblastoma. *Int. J. Mol. Sci.* **22**, 351. https://doi.org/10.3390/ijms22010351 (2020).
37. Roncevic, A. *et al.* Personalized treatment of glioblastoma: Current state and future perspective. *Biomedicines* **11**, 1579. https://doi.org/10.3390/biomedicines11061579 (2023).
38. Gaca-Tabaszewska, M., Bogusiewicz, J. & Bojko, B. Metabolomic and lipidomic profiling of gliomas—A new direction in personalized therapies. *Cancers* **14**, 5041. https://doi.org/10.3390/cancers14205041 (2022).
39. Longhitano, L. *et al.* Lactate modulates microglia polarization via IGFBP6 expression and remodels tumor microenvironment in glioblastoma. *Cancer Immunol. Immunother.* **72**, 1–20. https://doi.org/10.1007/s00262-022-03215-3 (2023).
40. Hassannia, B., Vandenabeele, P. & Vanden Berghe, T. Targeting ferroptosis to iron out cancer. *Cancer Cell* **35**, 830–849. https://doi.org/10.1016/j.ccell.2019.04.002 (2019).
41. Liu, N., Lin, X. & Huang, C. Activation of the reverse transsulfuration pathway through NRF2/CBS confers erastin-induced ferroptosis resistance. *Br. J. Cancer* **122**, 279–292. https://doi.org/10.1038/s41416-019-0660-x (2020).
42. Yu, Y. *et al.* The ferroptosis inducer erastin enhances sensitivity of acute myeloid leukemia cells to chemotherapeutic agents. *Mol. Cell Oncol.* **2**, e1054549. https://doi.org/10.1080/23723556.2015.1054549 (2015).
43. Tsoi, J. *et al.* Multi-stage differentiation defines melanoma subtypes with differential vulnerability to drug-induced iron-dependent oxidative stress. *Cancer Cell* **33**, 890-904.e5. https://doi.org/10.1016/j.ccell.2018.03.017 (2018).
44. Luis, G. *et al.* Tumor resistance to ferroptosis driven by Stearoyl-CoA Desaturase-1 (SCD1) in cancer cells and Fatty Acid Biding Protein-4 (FABP4) in tumor microenvironment promote tumor recurrence. *Redox. Biol.* **43**, 102006. https://doi.org/10.1016/j.redox.2021.102006 (2021).
45. Friedmann Angeli, J. P., Krysko, D. V. & Conrad, M. Ferroptosis at the crossroads of cancer-acquired drug resistance and immune evasion. *Nat. Rev. Cancer* **19**, 405–414. https://doi.org/10.1038/s41568-019-0149-1 (2019).
46. Koppula, P., Zhuang, L. & Gan, B. Cystine transporter SLC7A11/xCT in cancer: Ferroptosis, nutrient dependency, and cancer therapy. *Protein Cell* **12**, 599–620. https://doi.org/10.1007/s13238-020-00789-5 (2021).
47. Yang, W. S. & Stockwell, B. R. Synthetic lethal screening identifies compounds activating iron-dependent, nonapoptotic cell death in oncogenic-RAS-harboring cancer cells. *Chem. Biol.* **15**, 234–245. https://doi.org/10.1016/j.chembiol.2008.02.010 (2008).
48. Weaver, K. & Skouta, R. The selenoprotein glutathione peroxidase 4: From molecular mechanisms to novel therapeutic opportunities. *Biomedicines* **10**, 891. https://doi.org/10.3390/biomedicines10040891 (2022).
49. Camiolo, G. *et al.* Iron regulates myeloma cell/macrophage interaction and drives resistance to bortezomib. *Redox. Biol.* **36**, 101611. https://doi.org/10.1016/j.redox.2020.101611 (2020).
50. NaveenKumar, S. K., Hemshekhar, M., Kemparaju, K. & Girish, K. S. Hemin-induced platelet activation and ferroptosis is mediated through ROS-driven proteasomal activity and inflammasome activation: Protection by melatonin. *Biochim. Biophys. Acta Mol. Basis Dis.* **1865**, 2303–2316. https://doi.org/10.1016/j.bbadis.2019.05.009 (2019).
51. Xu, G., Wang, H., Li, X., Huang, R. & Luo, L. Recent progress on targeting ferroptosis for cancer therapy. *Biochem. Pharmacol.* **190**, 114584. https://doi.org/10.1016/j.bcp.2021.114584 (2021).
52. Parenti, R., Salvatorelli, L. & Magro, G. Anaplastic thyroid carcinoma: Current treatments and potential new therapeutic options with emphasis on TfR1/CD71. *Int. J. Endocrinol.* **2014**, 685396. https://doi.org/10.1155/2014/685396 (2014).
53. Magro, G. *et al.* Aberrant expression of TfR1/CD71 in thyroid carcinomas identifies a novel potential diagnostic marker and therapeutic target. *Thyroid* **21**, 267–277. https://doi.org/10.1089/thy.2010.0173 (2011).
54. Seibt, T. M., Proneth, B. & Conrad, M. Role of GPX4 in ferroptosis and its pharmacological implication. *Free Radic. Biol. Med.* **133**, 144–152. https://doi.org/10.1016/j.freeradbiomed.2018.09.014 (2019).
55. Hayano, M., Yang, W. S., Corn, C. K., Pagano, N. C. & Stockwell, B. R. Loss of cysteinyl-tRNA synthetase (CARS) induces the transsulfuration pathway and inhibits ferroptosis induced by cystine deprivation. *Cell Death Differ.* **23**, 270–278. https://doi.org/10.1038/cdd.2015.93 (2016).
56. Doll, S. *et al.* FSP1 is a glutathione-independent ferroptosis suppressor. *Nature* **575**, 693–698. https://doi.org/10.1038/s41586-019-1707-0 (2019).
57. Soula, M. *et al.* Metabolic determinants of cancer cell sensitivity to canonical ferroptosis inducers. *Nat. Chem. Biol.* **16**, 1351–1360. https://doi.org/10.1038/s41589-020-0613-y (2020).
58. Wang, H. *et al.* Emerging mechanisms and targeted therapy of ferroptosis in cancer. *Mol. Ther.* **29**, 2185–2208. https://doi.org/10.1016/j.ymthe.2021.03.022 (2021).
59. Longhitano, L. *et al.* Lactate rewrites the metabolic reprogramming of uveal melanoma cells and induces quiescence phenotype. *Int. J. Mol. Sci.* **24**, 24. https://doi.org/10.3390/ijms24010024 (2022).
60. Caruso, G. *et al.* Characterization of carnosine effect on human microglial cells under basal conditions. *Biomedicines* **11**, 474. https://doi.org/10.3390/biomedicines11020474 (2023).
61. Lazzarino, G. *et al.* Single-sample preparation for simultaneous cellular redox and energy state determination. *Anal. Biochem.* **322**, 51–59. https://doi.org/10.1016/j.ab.2003.07.013 (2003).
62. Giallongo, S. *et al.* Loss of macroH2A1 decreases mitochondrial metabolism and reduces the aggressiveness of uveal melanoma cells. *Aging* **12**, 9745–9760. https://doi.org/10.18632/aging.103241 (2020).
63. Xu, L. *et al.* Topography of transcriptionally active chromatin in glioblastoma. *Sci. Adv.* **7**, 4676. https://doi.org/10.1126/sciadv.abd4676 (2021).
64. Crielaard, B. J., Lammers, T. & Rivella, S. Targeting iron metabolism in drug discovery and delivery. *Nat. Rev. Drug Discov.* **16**, 400–423. https://doi.org/10.1038/nrd.2016.248 (2017).
65. Possemato, R. *et al.* Functional genomics reveal that the serine synthesis pathway is essential in breast cancer. *Nature* **476**, 346–350. https://doi.org/10.1038/nature10350 (2011).
66. Verba, K. A. & Agard, D. A. How Hsp90 and Cdc37 Lubricate Kinase Molecular Switches. *Trends Biochem. Sci.* **42**, 799–811. https://doi.org/10.1016/j.tibs.2017.07.002 (2017).
67. Yang, F. *et al.* Ferroptosis heterogeneity in triple-negative breast cancer reveals an innovative immunotherapy combination strategy. *Cell Metab.* **35**, 84-100.e8. https://doi.org/10.1016/j.cmet.2022.09.021 (2023).
68. Goldman, M. J. *et al.* Visualizing and interpreting cancer genomics data via the Xena platform. *Nat. Biotechnol.* **38**, 675–678. https://doi.org/10.1038/s41587-020-0546-8 (2020).

Acknowledgements
The authors acknowledge the confocal microscopy facility at the Bio-Nanotech Research and Innovation Tower (BRIT) of the University of Catania. This study was partially funded by the "Drug Delivery: veicoli per un'innovazione sostenibile" (code PON03PE_00216_1, CUP: B82F15000010005. Funder "Ministry of University and Research", ITALY) to R.P.; the Piano di Incentivi per la Ricerca di Ateneo 2020-2022, Linea di Intervento 2, "MD-RESETT-GLIO" to R.P.; the grant Piano di Incentivi per la Ricerca di Ateneo 2020-2022, Linea di intervento 3-Starting Grant, "CHRONOS" from the University of Catania to N.V.; the National Plan for NRRP Complementary Investments (PNC, established with the decree-law 6 May 2021, n. 59, converted by law n. 101 of 2021) in the call for the funding of research initiatives for technologies and innovative trajectories in the health and care sectors (Directorial Decree n. 931 of 06-06-2022)—project n. PNC0000003—AdvaNced Technologies for Human-centrEd Medicine (project acronym: ANTHEM). This work reflects only the authors' views and opinions, neither the Ministry for University and Research nor the European Commission can be considered responsible for them.

Author contributions
Conceptualization: S.D.A.; C.G.; N.V.; R.P.; Methodology: S.D.A.; S.D.; A.L.; S.C.; S.G.; F.T.; L.S.; Giacomo L.; A.M.A.; Investigation: S.D.A.; S.D.; A.L.; S.C.; S.G.; Data curation: S.D.A.; S.D.; C.G.; N.V.; Validation: S.D.A.; S.D.; A.L.; S.C.; F.T.; Giuseppe L.; G.M.; D.T.; M.L.; C.G.; N.V.; Formal analysis: S.D.A.; S.D.; A.L.; S.C; Giacomo L.; A.M.A.; Giuseppe L.; G.M.; D.T.; M.L.; C.G.; N.V.; R.P.; Resources: G.M.; D.T.; M.L.; C.G.; N.V.; R.P.; Writing-original draft: S.D.A.; S.D.; N.V.; Writing-review and editing: S.D.A.; S.D.; A.L.; S.C.; S.G.; F.T.; L.S.; Giacomo L.; A.M.A.; Giuseppe L.; G.M.; D.T.; M.L.; C.G.; N.V.; R.P.; Project administration: S.D.A.; C.G.; N.V.; R.P. All authors read and approved the final manuscript.

Competing interests
The authors declare no competing interests.

Additional information
Supplementary Information The online version contains supplementary material available at https://doi.org/10.1038/s41598-024-72024-8.

Correspondence and requests for materials should be addressed to C.G. or N.V.

Reprints and permissions information is available at www.nature.com/reprints.

Publisher's note Springer Nature remains neutral with regard to jurisdictional claims in published maps and institutional affiliations.